Simulation of Dynamic Particle Trajectories Through Resonant-Tunneling Structures Based upon Wigner Distribution Function

Hideaki Tsuchiya and Tanroku Miyoshi

Department of Electrical and Electronics Engineering
Kobe University, 1-1, Rokko-dai, Nada-ku, Kobe 657-8501, Japan
Phone & Fax: +81-78-803-1073
E-mail: tsuchiya@eedept.kobe-u.ac.jp

1. Introduction

Investigating transport in solids typically uses the Boltzmann equation, which has a natural particle interpretation. The particle concept of carriers is widely accepted in terms of particle Monte Carlo simulations where the motions of carriers are computed transiently in momentum and real spaces, subject to external forces due to applied electric and magnetic fields and given scattering mechanisms [1,2]. The obtained transient data stand for the particle trajectories in the phase space. On the other hand, the Wigner distribution function, which corresponds to a quantum probability distribution function, has been actively investigated on its formulations and practical applications to quantum effect devices [3-7]. In particular, Jensen and Buot reported the application of the Wigner distribution function to obtain a particle trajectory in resonant-tunneling diodes (RTDs) by utilizing the phase space description in the Wigner distribution function [5,6]. They succeeded in a convenient visualization of particle tunneling process and an estimation of tunneling times. However, their simulations were limited to small bias conditions and the correspondence with classical theory was not clear. In this paper, the dynamic particle trajectories of RTDs at large bias conditions are studied based upon the Wigner trajectory technique, and further the comparison between the Wigner and the classical trajectories is discussed.

2. Quantum Trajectories

The Wigner distribution function $f(x,k,t)$ is defined as the Fourier transform of the density matrix represented in the coordinate space with respect to the relative coordinate [3-6] or the energy-integral of the nonequilibrium Green's function [7-9]. Its time evolution is given by

$$\frac{\partial f}{\partial t}=-\frac{\hbar k}{m^*}\frac{\partial f}{\partial x}-\frac{1}{\hbar}\int_{-\infty}^{\infty}\frac{dk'}{2\pi}V(x,k-k')f(x,k',t)+\left(\frac{\partial f}{\partial t}\right)_C, \quad (1)$$

where

$$V(x,k)=2\int_0^{\infty}d\xi\sin(k\xi)\left[v\left(x+\xi/2\right)-v\left(x-\xi/2\right)\right], \quad (2)$$

where $v(x)$ denotes the potential energy profile, and the effective mass m^* is assumed to be constant throughout the device. The third term on the right-hand side of eq. (1) represents the collision term. The motion of the phase space trajectories are defined by writing eq. (1) in the form of a total time derivative as follows.

$$\frac{\partial f}{\partial t}=-\frac{dx}{dt}\frac{\partial f}{\partial x}-\frac{dk}{dt}\frac{\partial f}{\partial k}+\left(\frac{\partial f}{\partial t}\right)_C. \quad (3)$$

Comparing eq. (3) with eq. (1), the velocity of the particles and the force acting on the particles are respectively given by [5,6]

$$\frac{dx}{dt} = \frac{\hbar k}{m^*}, \quad (4)$$

$$\frac{dk}{dt} = \frac{\frac{1}{\hbar}\int_{-\infty}^{\infty}\frac{dk'}{2\pi}V(x,k-k')f(x,k')}{\partial f/\partial k}\equiv\frac{F_{eff}(x,k)}{\hbar}. \quad (5)$$

First, the particle velocity (4) is as expected. On the other hand, eq. (5) denotes that the particles evolve according to the effective quantum forces F_{eff}. Far from the quantum structures, where the potential is smoothly varying, eq. (5) reduces to the classical one, $dk/dt = -1/\hbar(dv/dx)$, and therefore the classical description is regained. As the particles approach the quantum regions where the potential changes abruptly, their trajectories are updated by the quantum force given in eq. (5). We can obtain the dynamics of the phase space trajectories by calculating the Wigner function $f(x,k)$ and the potential energy $v(x)$, and from it, $x(t)$ and $k(t)$ by

$$x(t+\delta t) = x(t)+\frac{\hbar k(t)}{m^*}\delta t, \quad (6)$$

$$k(t+\delta t) = k(t)+\frac{F_{eff}(x(t),k(t))}{\hbar}\delta t, \quad (7)$$

0-7803-4369-7/98 $10.00

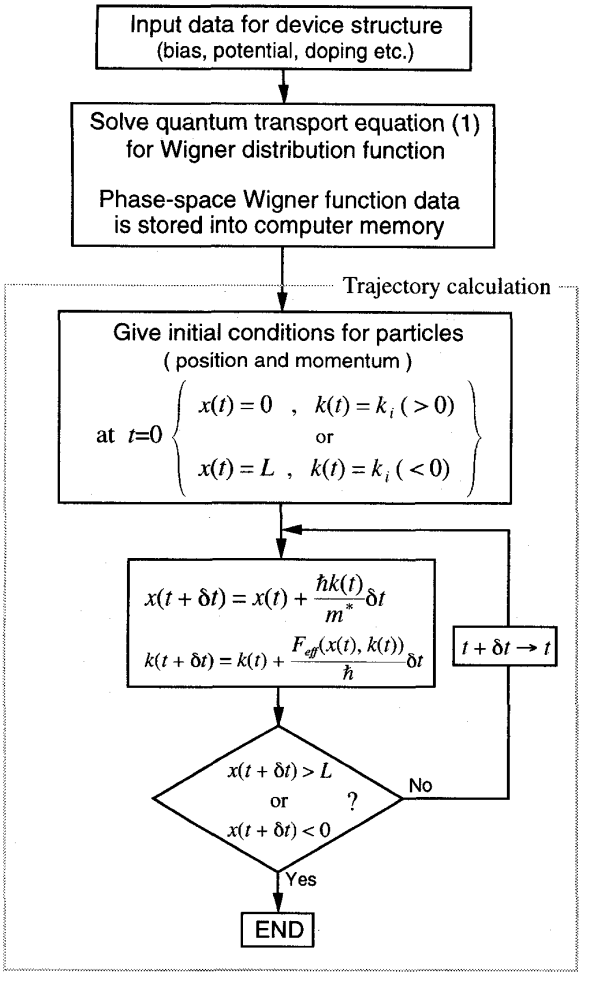

Figure 1: Flow chart for Wigner trajectory calculation.

where δt is the time interval. Fig.1 shows the flow chart of our trajectory calculation. First, the quantum transport equation (1) for the Wigner distribution function is numerically solved for the given device structure [3-6], and then the Wigner distribution function data in the phase space are stored into the computer memory. Now, the trajectory calculation is started. First of all, the initial conditions of particles with respect to position and momentum are given, where L denotes the device length. Here, we assign the positive momentum ($k > 0$) at the left boundary and the negative momentum ($k < 0$) at the right boundary, respectively, in order to represent the particles injected toward the double barrier structure. Next, let those particles move in the phase space according to eq. (6) and (7) during the time interval δt. Since the particles move fast in the real space at the large bias conditions, the time interval δt should be small enough ($\simeq$1fs) compared to the flight time across one mesh-spacing in the x-coordinate. This calculation will be continued until the particles reach the device boundaries, $x = 0$ or $x = L$. The obtained transient data stand for the particle quantum trajectories in the phase space.

As Jensen and Buot pointed out [5], the above concept of the effective quantum force is analogous to the Bohm trajectory in terms of quantum potential [10]. They also indicated that the velocity of the Bohm trajectory is represented by the average velocity of the Wigner trajectories. The Wigner trajectory technique has been examined for tunneling problems such as RTD [5] and field emission [6]. In particular, Jensen and Buot succeeded in a visualization of particle tunneling process in RTDs at small bias conditions. In this paper, we studied the dynamic particle trajectories of RTDs at large bias conditions based upon the Wigner trajectory technique, and further discussed the correspondence between the Wigner and the classical particle trajectories.

3. Dynamic Particle Trajectories of RTD

The simulation model of the RTD consists of two 2.8nm-$Al_{0.3}Ga_{0.7}As$ barriers and a 4.5nm-GaAs quantum well. The temperature is assumed to be 300K. Fig. 2 (a) shows the current-voltage characteristics of the double-barrier RTD. Fig. 2 (b) and (c) show the computed phase space trajectories of the double-barrier RTD at the bias voltages of (b) V=0.05V and (c) 0.12V, respectively, where any scattering and space-charge effects are neglected. The vertical lines represent the location of the potential barriers. Fig. 2 (c) corresponds to the current peak of the $I - V$ curve. Such dynamic particle trajectories at the large bias conditions are successfully evaluated in this study. First, for low momentum states the trajectories are reflected well before the barrier edge, which indicates the nonlocal quantum effects due to the potential barriers. Tunneling trajectories are observed for $k > 0.34\text{nm}^{-1}$ and $k > 0.15\text{nm}^{-1}$ in Fig. 2 (b) and (c), respectively. At the higher bias voltage, the tunneling trajectories occur for smaller momentum states. This corresponds to the shift of the transmission coefficient peak energy toward the lower momentum region by increasing the bias voltage. For reference, the transmission coefficient spectra are shown in the insets of Fig. 2 (b) and (c). In addition, the momenta of those tunneling trajectories are found to increase in the right electrode, which means the gain of extra kinetic energy from the potential energy difference. On the contrary, the tunneling trajectories incident from the right electrode with $k \sim -0.5\text{nm}^{-1}$ are loosing those kinetic energies after tunneling into the left electrode. Another interesting feature is that the trajectories incident from the right electrode with $k \sim -0.4\text{nm}^{-1}$ are penetrating the right barrier to change the direction inside the central quantum well.

Further, the Wigner trajectory technique allows us to

discuss the steady-state tunneling times. Fig. 3 shows the plot of position as a function of time for the trajectories shown in Fig. 2. The horizontal lines represent the location of the potential barriers. The velocity at any position is given by the slope at that position. It is found in Fig. 3 that the trajectories begin to speed down before reaching the first barrier and tunnel through the double-barrier region as they are gradually accelerated. At the higher bias, the particles tunnel out of the double-barrier region more rapidly than the lower bias case. However, it takes longer times for the particles to reach the first barrier at the higher bias. This is because the initial velocities of the tunneling trajectories are reduced at the higher bias condition due to the shift of the transmission coefficient peak energy toward the lower momentum region as shown in the inset of Fig. 2 (c).

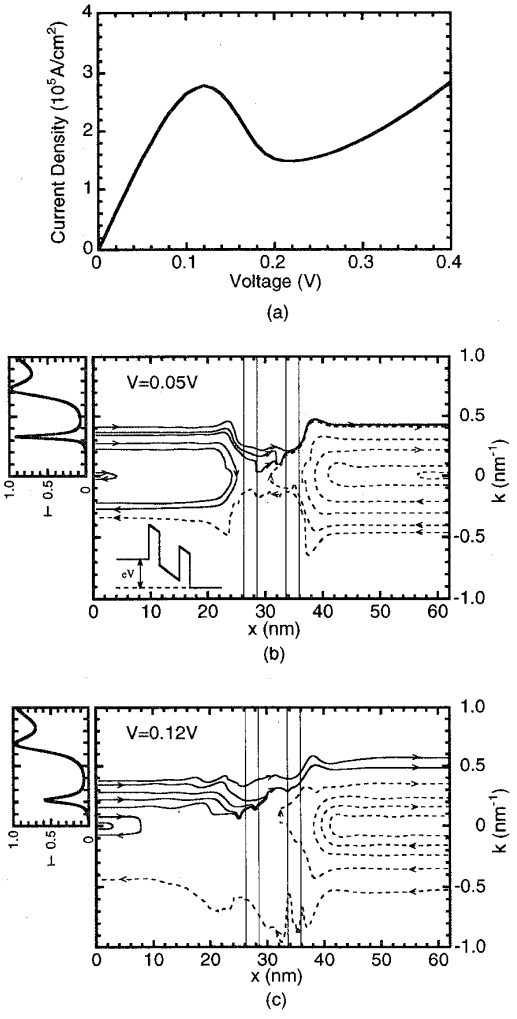

Figure 2: (a) Current-voltage characteristics of RTD. (b) and (c) shows the computed phase space trajectories at the bias voltages of 0.05V and 0.12V, respectively. The vertical lines represent the location of potential barriers. The insets show the corresponding transmission coefficient spectra.

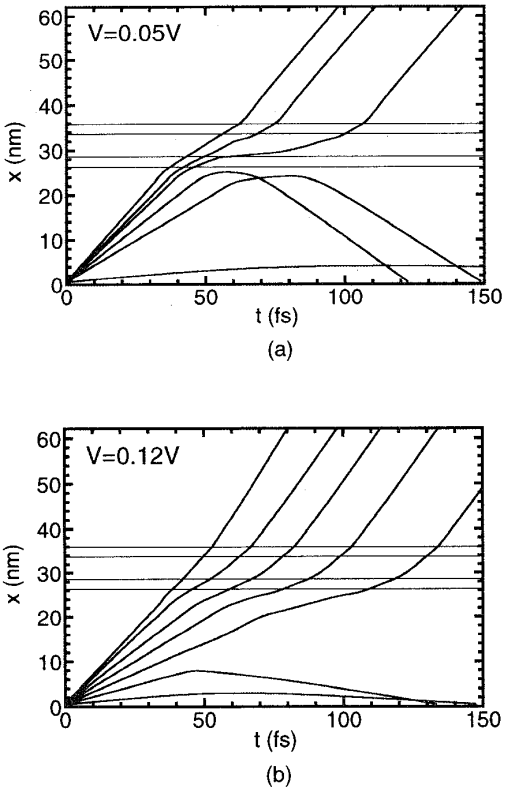

Figure 3: Plot of position as a function of time for trajectories shown in Fig. 2. The horizontal lines represent the location of potential barriers. The velocity at any position is given by the slope at that position.

4. Comparison between Wigner and Classical Trajectories

In this chapter, we compare the Wigner trajectories with the classical ones, to make clear the behavior of the tunneling trajectories. The classical trajectories correspond to the conventional Monte Carlo simulation and they are calculated by using $dk/dt = -1/\hbar(dv/dx)$ instead of eq. (5). As a matter of course, no quantum mechanical effects are included in the classical trajectories. Fig. 4 shows the comparison between the Wigner and classical trajectories at the bias voltages of (a) 0.05V

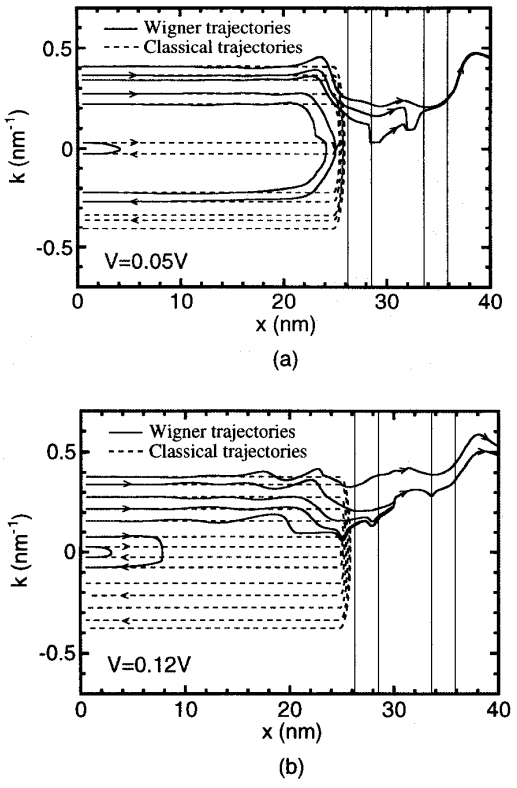

Figure 4: Comparison between Wigner and classical trajectories at bias voltage of (a) 0.05V and (b) 0.12V. Only the particle trajectories incident from the left electrode are plotted.

and (b) 0.12V. Only the trajectories incident from the left electrode are plotted. The influence of the effective quantum force is clearly indicated in Fig. 4. First, far from the double-barrier structure, where the potential is constant, the both trajectories are identical. This is due to the fact that the classical description is regained there as mentioned in the chapter 2. On the other hand, as the particles approach the double barrier region, the Wigner trajectories are modified to be reflected apart from the left barrier and tunnel through the double barrier under the influence of the effective quantum force. In the classical trajectories plotted in the dashed lines, all particles are reflected just before the left barrier. In addition, the classical trajectories are independent of the bias voltage, while the Wigner trajectories considerably change with the bias due to the variation of the transmission coefficient spectra shown in Fig. 2.

5. Conclusion

In this paper, the dynamic particle trajectories of the resonant-tunneling structure at the large bias conditions are investigated based upon the phase space description in the Wigner distribution function. The procedure for the Wigner trajectory calculation was presented in detail. We demonstrated the dynamic behaviors of the quantum tunneling trajectories and the steady-state tunneling times, corresponding with the transmission coefficient spectra and the classical particle trajectories. The Wigner trajectory technique presented in this paper can provide an instructive description of carrier nonequilibrium quantum transport distinct from the conventional carrier statistics such as carrier density and current density distributions. Thus, it will be available to understand the dynamic behaviors of various nanostructure devices.

References

1. W. Fawcett, A. D. Boardman, and S. Swain: J. Phys. Chem. Sol. **31** (1970) 1963.
2. C. Jacoboni and L. Reggiani: Rev. Mod. Phys. **55** (1983) 645.
3. W. R. Frensley: Phys. Rev. B **36** (1987) 1570.
4. N. C. Kluksdahl, A. M. Kriman, and D. K. Ferry: Phys. Rev. B **39** (1989) 7720.
5. K. L. Jensen and F. A. Buot: IEEE Trans. on Electron Devices **ED-38** (1991) 2337.
6. K. L. Jensen and A. K. Ganguly: J. Appl. Phys. **73** (1993) 4409.
7. G. D. Mahan: Phys. Rep. **145** (1987) 251.
8. F. A. Buot and K. L. Jensen: Phys. Rev. B **42** (1990) 9429.
9. H. Tsuchiya and T. Miyoshi: J. Appl. Phys. **83** (1998) 2574.
10. D. Bohm: Phys. Rev. **2** (1952) 166.